Microstructure and Mechanical Properties of Gas-Tungsten-Arc–Welded Ti-15-3 Beta Titanium Alloy

K. BALACHANDAR, V. SUBRAMANYA SARMA, BHANU PANT, and G. PHANIKUMAR

Microstructure and mechanical properties of gas-tungsten-arc (GTA)–welded Ti-15V-3Cr-3Sn-3Al alloy in direct current electrode negative mode are characterized. The thermal profile was measured during welding with continuous current (CC) and pulsed current (PC) at different frequencies. A single-step postweld aging of the welded samples at subtransus temperature was attempted to study precipitation of alpha phase. Two different morphologies of alpha phase are observed along with a partitioning of alloying elements into the two phases. Processing conditions for higher strength are identified and correlated with the thermal profile. Microstructure changes due to postweld heat treatment were characterized.

DOI: 10.1007/s11661-009-9952-8

I. INTRODUCTION

BETA titanium alloys are used in aerospace and automotive sectors due to high specific strength, good hardenability, and excellent corrosion resistance.[1] These alloys are heat treatable and possess excellent cold working capabilities in the solution-treated condition.[1,2] Currently, key components fabricated from β titanium alloys have found applications in many fields such as aerospace, automotive, biomedical, sporting, and construction.[3]

Pure titanium transforms from hcp (α) to bcc (β) structure above 882 °C.[4] Alloying elements such as Mo, V, Nb, and Cr stabilize the bcc structure by lowering the transformation temperature significantly and are termed as β stabilizers. In general, a molybdenum equivalency[5] of 10 pct is required to stabilize the β phase upon quenching. The nominal composition of the alloy used for this study, Ti-15V-3Cr-3Al-3Sn (Ti-15-3 alloy), has a molybdenum equivalency of 11.85 pct and is thus able to retain the bcc structure at room temperature.

Gas-tungsten-arc welding (GTAW) with pulsed current (PC) technique has several advantages, including grain-refined fusion zone (FZ), reduced width of heat-affected zone (HAZ), and compositional homogeneity. This technique involves cycling the welding current between peak current (to melt the base material (BM)) and base current (to maintain a stable arc) at a regular frequency. Unlike continuous current (CC), half of the pulsing cycle is used for heating and the other half for heat dissipation and the width of the HAZ is reduced. Extensive work has been reported about the effect of pulsing current on microstructure and properties of weldments of several materials such as aluminum alloys,[6–8] austenitic stainless steels,[9,10] and titanium α-β alloys,[11–13] Becker *et al.*[14] and Baeslack III *et al.*[15] have studied GTA weld solidification and HAZ liquation phenomena in metastable β titanium alloy, β-21S. There is no study reported in the open literature on the effect of pulsing frequency in comparison with CC on Ti-15-3 alloy.

Metastable β-Ti alloys can be heat treated at subtransus temperatures for prolonged time periods to form α and ω phases in the β matrix. It has been established that $T\omega$, the temperature at which the β-ω transformation is initiated, decreases rapidly with increasing solute additions.[16] The high solute content of Ti-15-3 alloy and high cooling rates in welding preclude formation of the ω phase.[1,17] The strengthening of Ti-15-3 is attributed to the precipitation of uniformly dispersed fine α phase in the β matrix.[18] Solutionizing and aging results in α precipitation within the β grains.[19,20] The morphology of the α phase is influenced by the aging temperature, duration, and amount of α stabilizers present in the alloy. The morphology, size, and distribution of these precipitates affect the mechanical properties of the alloy. Homogeneous precipitation of a fine α phase in metastable β-Ti alloys leads to increased yield strength (YS) and lowers ductility. Previous studies on duplex aging have shown that useful strengths could be achieved at the cost of its fracture toughness through a sequence of aging at low temperature and then at higher temperature.[21–23] The combination of lower aging temperature followed by a higher aging temperature appears to be more successful in improving the toughness.[24] With a metastable β phase at room temperature, Ti-15-3 alloys could be cold rolled[25] and further aged in a single step also.[26]

Due to their excellent cold formability, the main applications of Ti-15-3 alloys are in fabrication from

K. BALACHANDAR, Research Student, and V. SUBRAMANYA SARMA and G. PHANIKUMAR, Assistant Professors, are with the Department of Metallurgical and Materials Engineering, Indian Institute of Technology Madras, Chennai 600036, India. Contact e-mail: gphani@iitm.ac.in BHANU PANT, Head, Materials Processing Division, is with the Vikram Sarabhai Space Center, Thiruvananthapuram 695 022, India.

Manuscript submitted February 20, 2009.
Article published online August 26, 2009

as-rolled strips. Also, cold formability in the solution-treated condition coupled with amenability for strengthening after final aging renders this alloy suitable for low-cost high-strength pressure vessels for space applications. Most of the applications invariably involve a welding step (GTAW/electron beam welding (EBW)) during processing. During GTAW, the HAZ undergoes a thermal cycle that could lead to precipitation of the α phase and affect the mechanical properties of the as-welded joint. This study is aimed at characterizing the microstructural changes during welding as well as after postweld heat treatment and the resulting mechanical properties of the weldment. In the present work, the heat treatment cycle that the HAZ undergoes is characterized by an *in-situ* thermal profile measurement using multiple thermocouples. The pulse frequency is varied as the control parameter keeps the rest of the parameters constant. In order to study the relationship between the aging temperature and the resulting microstructural modification, a set of aging treatments from 480 °C to 540 °C for 10 hours were carried out on the welded specimen. We present results only for an optimum aging temperature 520 °C for brevity. The selection of the aging temperature range for this alloy is based on aging studies[26] on a wide range of metastable β titanium alloys.

II. EXPERIMENTS

A. *Welding Experiments*

Autogenous bead-on-plate welds were made using the GTAW process with an argon gas trail environment (argon flow in torch = 20 L/min and in backup and trail = 23 L/min) over the weldment. This trail environment involves the use of multiple gas jets directed at the surface of the weld pool to protect the weldment from being contaminated by atmospheric gases such as oxygen and nitrogen. This environment also increases the convective heat transfer on the surface of the weld pool. All welding variables (weld speed: 150 mm/min, and voltage: 13.6 V) other than the current (CC 150 A, PC peak current 190 A, and base current 110 A), in the case of the PC technique, maintained the same order to keep the heat input (816 J/mm) constant in all cases.

Simultaneous temperature measurements at five locations away from the FZ were made *in situ* using Pt-Pt/Rh thermocouples during each of the welding experiments. The hot junctions of Pt-Pt/Rh thermocouples were tight fixed on the top surface of the plates at a distance of 7, 9, 11, 13, and 15 mm perpendicular to the weld centerline. These distances are chosen after estimating the width of the FZ to ensure that the thermocouples were located in the HAZ. The thermocouples were connected to a data acquisition system *via* a signal conditioner, and temperatures were recorded from each thermocouple at a sampling rate of 100 samples per second per junction.

The welded samples were mechanically polished through 1000 grit SiC papers and etched with Kroll's reagent. Postweld heat treatment was performed on one set of weld samples encapsulated in an evacuated quartz crucible. The results shown are for samples heat treated at 520 °C for 10 hours and air cooled.

B. *Characterization*

The bulk composition of the alloy was confirmed with inductively coupled plasma–optical emission spectrometry as well as energy-dispersive X-ray analysis (EDAX) (used with scanning electron microscopy (SEM)). The BM revealed (all in wt pct) 77.35Ti, 13.73V, 3.47Al, 1.93Cr, and 3.52Sn. The BM is taken as 5-mm-thick as-rolled sheets of 150 mm × 150 mm for the welding experiments. The microstructure of the BM is shown in Figure 1. The BM microstructure shows that the average grain size was about 40 μm and the hardness was ~300 HV_{500g}. The grain aspect ratio (GAR) is found to be around 3 with a longer dimension along the rolling direction.

The welded samples were characterized using optical and electron microscopy. Secondary electron (SE) imaging, backscattered electron imaging, and compositional analysis were carried out on an FEI Quanta200 scanning electron microscope (JEOL Ltd., Tokyo, Japan) interfaced with an EDAX and TSL-OIM EBSD analysis system. Extensive transmission electron microscopy (TEM) was performed using a PHILIPS* CM12 microscope with selected area diffraction and measurement of local compositions using an EDAX attachment. To analyze the phase content, X-ray diffraction was conducted on the samples using a Bruker D8 diffractometer (Bruker AXS GmbH, Karlsruhe, Germany) with Cu K_α radiation.

A microhardness survey was conducted across the welded sample. Uniaxial transverse tensile tests were conducted at room temperatures on as-welded samples using an MTS 100kN servohydraulic system. Electrodischarge wire cutting was used to prepare the specimens per ASTM E-8-04 standard. Three tests were performed for each welding condition.

*PHILIPS is a trademark of Philips Electronic Instruments Corp., Mahwah, NJ.

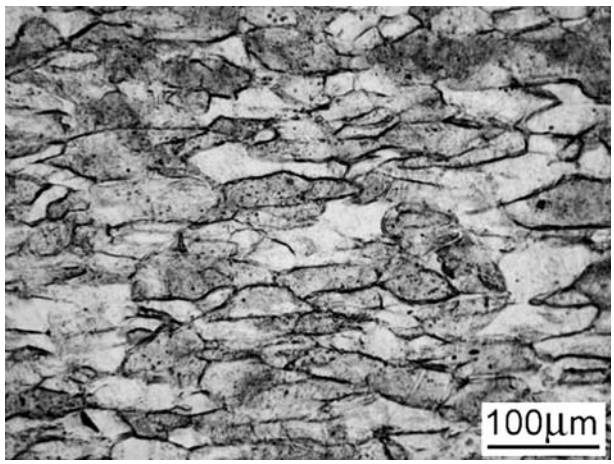

Fig. 1—Optical microstructure of the BM.

For detailed characterization, larger samples of HAZ were obtained using a thermomechanical simulator by employing the same thermal cycle as determined using the actual welding experiments. Thermal simulation of the HAZ thermal cycle was conducted using a thermomechanical simulator, Gleeble 1500D (Dynamic Systems Inc., Poestenkill, NY). The sample size chosen was 120 mm × 10 mm × 3 mm.

III. RESULTS

Figure 2 shows temperature profiles recorded by thermocouples at a distance of 9 mm from the weld centerline for all the welding conditions. The peak temperature reached as well as the heating and cooling rates are seen to be highest for the 4 Hz sample. Minor fluctuations in the heating and cooling rates at temperatures below 400 °C are due to the protective argon hood. Since the trailing end is focused (10 L/min flow of argon), there is a reduced cooling rate toward the end of the welding.

The welding torch moves along the predetermined line, and when it surpasses the thermocouple location, the cooling rate decreases. There is a slower cooling rate at lower temperatures since the argon flow is cut off beyond a distance from the welding torch that corresponds to roughly 300 °C. The same effect is felt in the case of the pulsed frequency welded specimen also, but with fluctuations in the heating rate, which reflect the effect of pulsing frequency.

Peak temperatures recorded by each thermocouple in a given experiment are plotted against the location of the thermocouple to obtain the temperature gradient in the heat-affected region. The data as shown in Figure 3 show a large thermal gradient of about 150 °C/mm in the region.

The microstructure of the weldment from the FZ to the BM is shown in Figure 4. The white dots indicate the fusion line. One can note that the grain size in the HAZ adjacent to the fusion line is larger (~160 μm) than that in the same region adjacent to the BM where it is as fine as 60 μm. The grain size at the center of the HAZ is 105 μm. The average GARs in the HAZs for different welding conditions and BM are shown in Figure 5. One can note that in all welding conditions, the grains in the HAZ are equiaxed. In contrast, the FZ grain size is around 640 μm with a GAR of 2.2.

Figure 6 shows a piecewise linear thermal profile that closely matches the experimentally determined thermal profile experienced by the HAZ. This linearized thermal

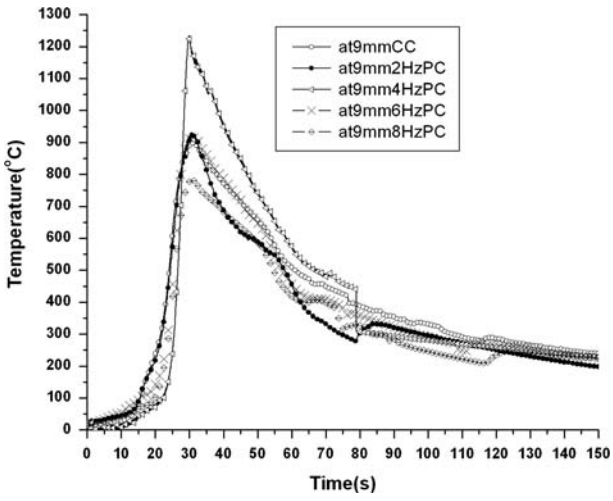

Fig. 2—The actual weld thermal cycles measured at 150 mm/min speed and at 9 mm from weld centerline.

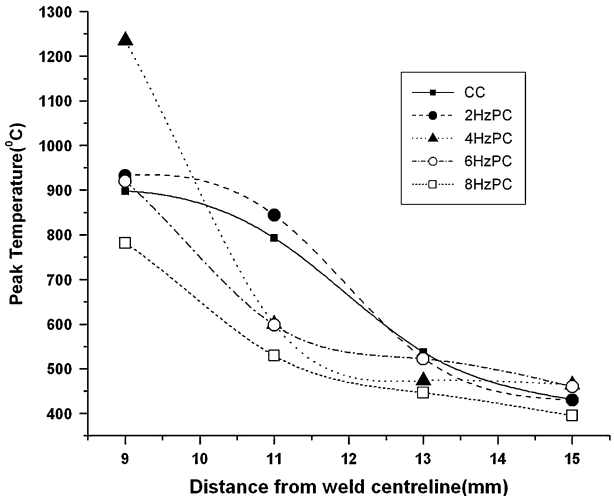

Fig. 3—Peak temperature measured at different distances from weld centerline.

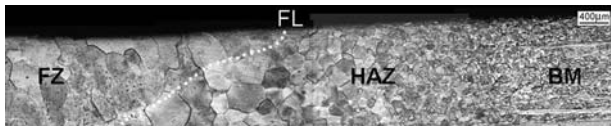

Fig. 4—Microstructure of the weldment from the FZ to the BM (dotted line indicates the fusion line).

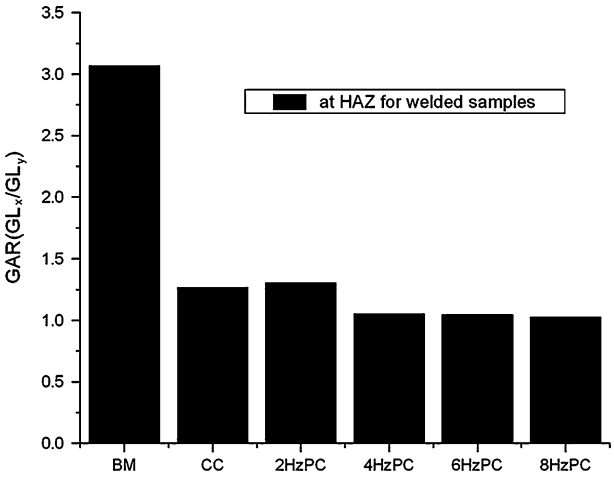

Fig. 5—Comparison of GAR of BM and welded samples.

profile is used in the thermomechanical simulator to obtain larger samples of the same thermal history as the HAZ for detailed characterization. The HAZ microstructure of an actual weldment (Figure 7(a)) and thermally simulated one (Figure 7(b)) closely match. The average grain sizes (~75 to 125 μm) have also been confirmed to be similar.

Secondary electron images from SEM did not reveal any contrast of the α phase in the weldments. However, detailed TEM revealed thin plates of α precipitate grown from β grain boundaries in the weldments. Figure 8 shows the bright-field images and selected area diffraction patterns of a CC weld sample (Figure 8(a)) and a pulse current (PC) weld sample (Figure 8(b)). The CC FZ shows the bright-field image of strained β matrix in the [001] zone. The electron diffraction pattern taken from the corresponding region shows streaks but no maxima. However, the PC FZ indicates few maxima in the diffraction pattern and the presence of α, as seen in the bright-field image in the [0001] zone. The arrows in the corresponding selected area electron diffraction (SAED) pattern indicate extra spots corresponding to β matrix. The spacing of α plates is around 50 nm. The orientation relationship, as noticed in the superimposed diffraction patterns in the region, is $[023]_\beta \parallel [0001]_\alpha$.

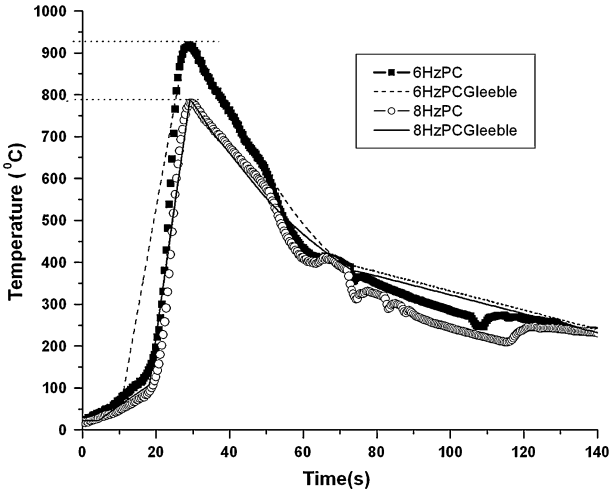

Fig. 6—Simulated weld thermal compared with that of actual thermal cycles measured at 150 mm/min speed and at 9 mm from weld centerline.

A microhardness survey across the entire weldment (Figure 9) showed significant scatter that is most likely due to the inhomogeneous precipitation. However, certain trends can be noticed. The FZ of CC weldment shows significant softening. Pulsed current weldments are generally stronger than CC weldments of the same heat input. The maximum strength observed corresponds to the 4 Hz sample. This is also reflected in the uniaxial tensile tests, which are shown in Table I. The transverse test specimens contain the FZ at the center of the gage length and the HAZ followed by BM on either end of the gage length. Failure was observed in the FZ for all samples (Figure 10(b)). As can be noted, the CC weld sample shows the lowest strength, lower than even the BM. The elongation is more than 17 pct for all the samples. The 4 Hz weldment shows a strength improvement of about 50 pct when compared to the CC weldment. Figure 10 also shows tensile property evaluation for the 4 Hz PC weldment after postweld heat treatment at 520 °C for 10 hours. There is significant improvement in the strength with a loss in ductility. Figure 10(b) shows that failure occurred in the BM for the postweld heat-treated sample.

Figures 11(a) and (b) show bright-field transmission electron images of the FZ and HAZ of the weldment pulsed with 4 Hz PC. The FZ shows finely spaced plates corresponding to early stage precipitation of α. Strained regions could also be seen with a line of no contrast parallel to the length of the platelets. The HAZ shows β grains with similar finely spaced α platelet contrast. The spacing of these patterns is seen to be much smaller than the spacing of α plates of, *e.g.*, 8 Hz sample.

Postweld heat-treated samples (aged at 520 °C for 10 hours) are also characterized in detail. Figure 12

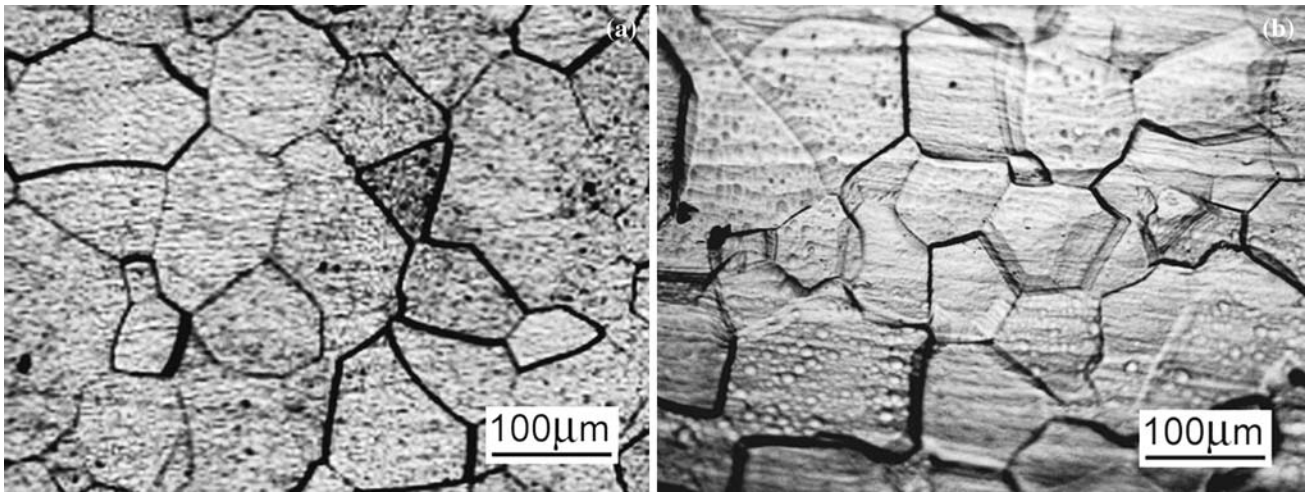

Fig. 7—Optical micrographs at 9 mm from the WC of (*a*) experimental and (*b*) simulated HAZ.

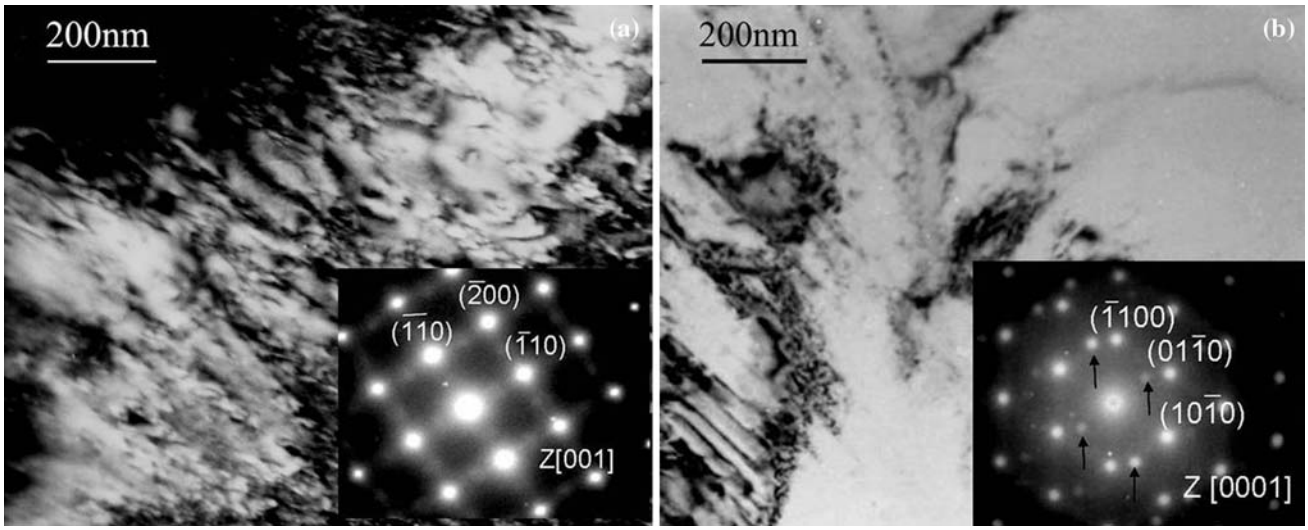

Fig. 8—Transmission electron micrograph and SAED pattern of (*a*) CC-FZ, beta matrix [001] showing streaks of transformation product, and (*b*) 8HzPC-FZ showing the presence of transformation product, alpha [0001] in retained beta matrix (indicated by arrows). The dark regions correspond to alpha phase, and the bright background corresponds to beta phase.

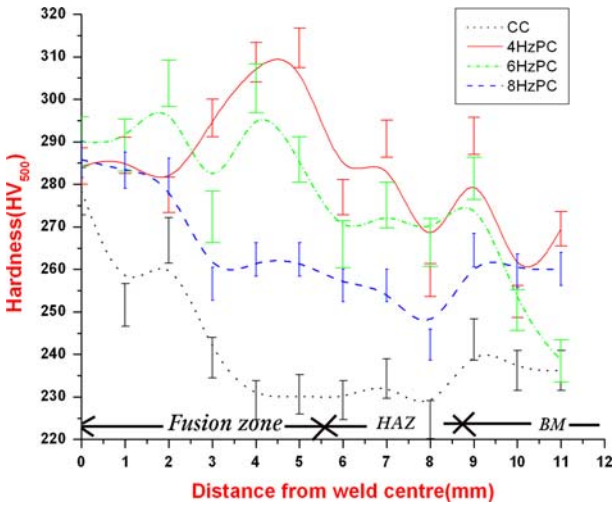

Fig. 9—Microhardness across the weldments from weld centerline.

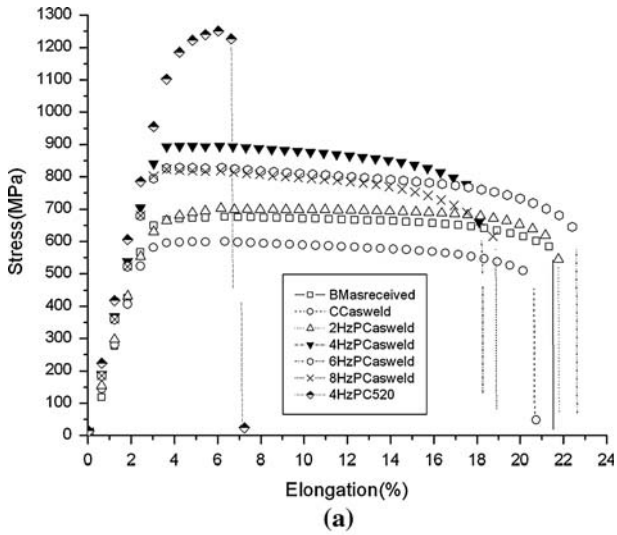

Fig. 10—(*a*) Stress-strain curves from uniaxial tensile test of the as-received, welded, and postweld aged specimen (4HzPC/520 °C). (*b*) Photograph of 4HzPC as-welded and postweld aged fractured samples.

Table I. Tensile Properties of GTAW Samples

Condition	YS (MPa)	Ultimate Tensile Strength (MPa)	Percent Elongation (25-mm GL)
BM	657 ± 8	674 ± 10	21.5 ± 2
CC	586 ± 9	600 ± 14	20.6 ± 2
2Hz-PC	687 ± 7	702 ± 13	21.7 ± 1
4Hz-PC	875 ± 6	897 ± 7	18.3 ± 2
6Hz-PC	815 ± 7	829 ± 9	22.6 ± 1
8Hz-PC	806 ± 9	823 ± 14	18.9 ± 1
4HzPC aged	1236 ± 16	1253 ± 13	7 ± 0.25

shows the SE image of deeply etched samples of postweld heat-treated condition. The contrast due to α formation at the grain boundary is discernible.

Figure 13 shows the precipitation of α phase in the interior of the β grains. Almost all the grains show lath-shaped α precipitates. These grains show longer laths of

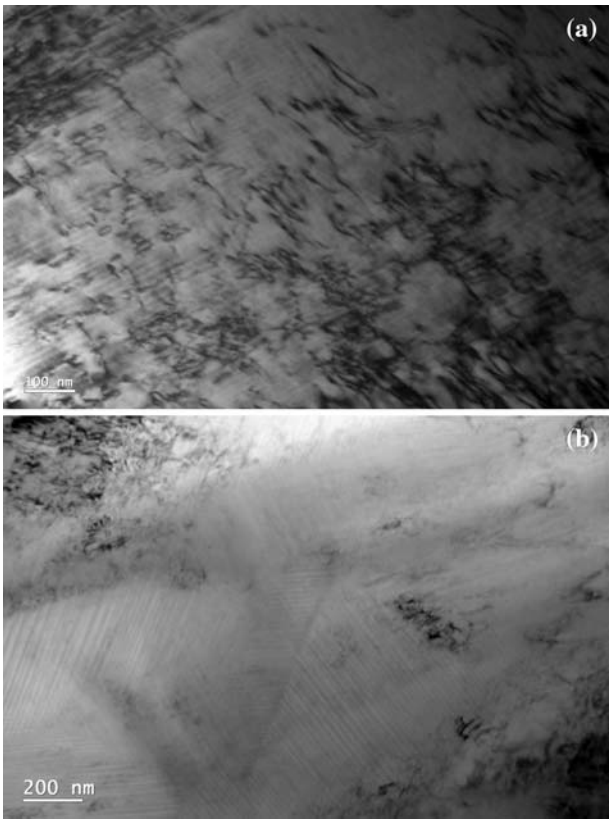

Fig. 11—TEM of the 4HzPC as-welded sample (*a*) FZ and (*b*) HAZ. The dark regions correspond to alpha phase, and the bright background corresponds to beta phase.

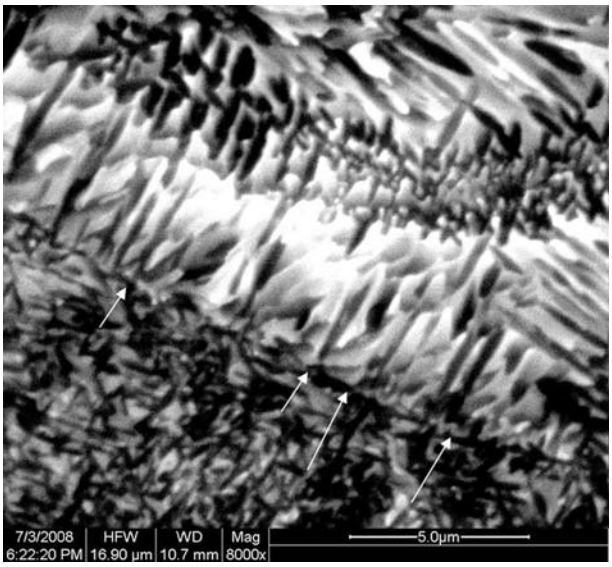

Fig. 12—SE micrograph showing allotriomorphs, α_{GB} (large arrows), along the prior β-grain boundary (small arrows).

α precipitation through the entire width of the grain, and also fine distribution of α in the β matrix is observed along the grain interior. Aged samples reveal the presence of transformed phase β' well distributed all along the prior β grains. The TEM micrographs show that the α precipitates are relatively shorter and smaller in the HAZ of 4 Hz PC-aged samples (Figure 13(a)) as compared to similar areas of 6 Hz PC-aged samples (Figure 13(b)).

IV. DISCUSSION

A. *HAZ Microstructure*

The thermal diffusivity of β titanium is low, *viz.* ($D = 3.44 \times 10^{-6}$ m^2/s at room temperature).[27] The PC weld experiments are performed at different values of pulse frequency (n) with 50 pct of the cycle time at peak current and the rest 50 pct at base current, at a constant torch velocity of V. Thus, the diffusion distance for the melting portion of each cycle scales as $\sqrt{D/n}$, whereas the torch travels a distance V/n. Since the velocity used in the experiments is 2.5 mm/s, we note that it is for 4 Hz that the two scales are closest to each other such that the HAZ receives sensible heat from the peak portion of each current pulse of the moving torch in a manner that accumulates the heat. At higher pulse frequencies, the diffusion length scale is much larger so that the HAZ experiences sensible heat from the moving heat source in a time-averaged manner. Thus, the thermal profiles of high pulse frequency welds approach those measured in CC welds. At the lowest pulse frequency, the temperature in the HAZ shows fluctuations with matching frequency as also corroborated by the measured thermal profiles (not shown here). Thus, at the torch velocity used in this study, 4 Hz PC welding leads to the highest peak temperature in the HAZ as well as the maximum thermal gradient away from the fusion line.

The BM is in the as-rolled condition with the final rolling pass inducing a strain of 0.28 after annealing. Due to the thermal cycle imposed on the HAZ, one would expect recrystallization to take place. The decrease in GAR from about 3 in BM to about 1 in HAZ for all conditions confirms the same. Apart from recrystallization, grain growth is also expected in regions closest to the fusion line. The sharp thermal gradient across the HAZ also agrees with the gradient in grain size from the fusion line end to the BM end of the HAZ (Figure 4). Thus, we have the following sequence of microstructure across the weldment: elongated grains in BM $\rightarrow$ fine recrystallized equiaxed grains in HAZ $\rightarrow$ coarse recrystallized equiaxed grains in HAZ $\rightarrow$ FZ.

Noticing that the peak temperature corresponding to the location where the HAZ ends is about 400 °C (T_o), one can measure the duration for which the two ends of the HAZ are exposed to temperatures above T_o. The ratio of this duration near the FZ to near the BM is about 2.5. Quantitative comparison of the observed grain sizes is not attempted here. However, it is worth mentioning that an estimation of recrystallized grain size under continuous annealing of cold-rolled strips (after 80 pct strain) of the same material[28] at a temperature T and time τ gives an expression for the final grain size in μm as $D(T,\tau) = 0.8 \times 10^4 \tau^{0.24} \exp(-1.5 \times 10^4 / \mathrm{R}T)$, where R is the universal gas constant. The grain size in the HAZ

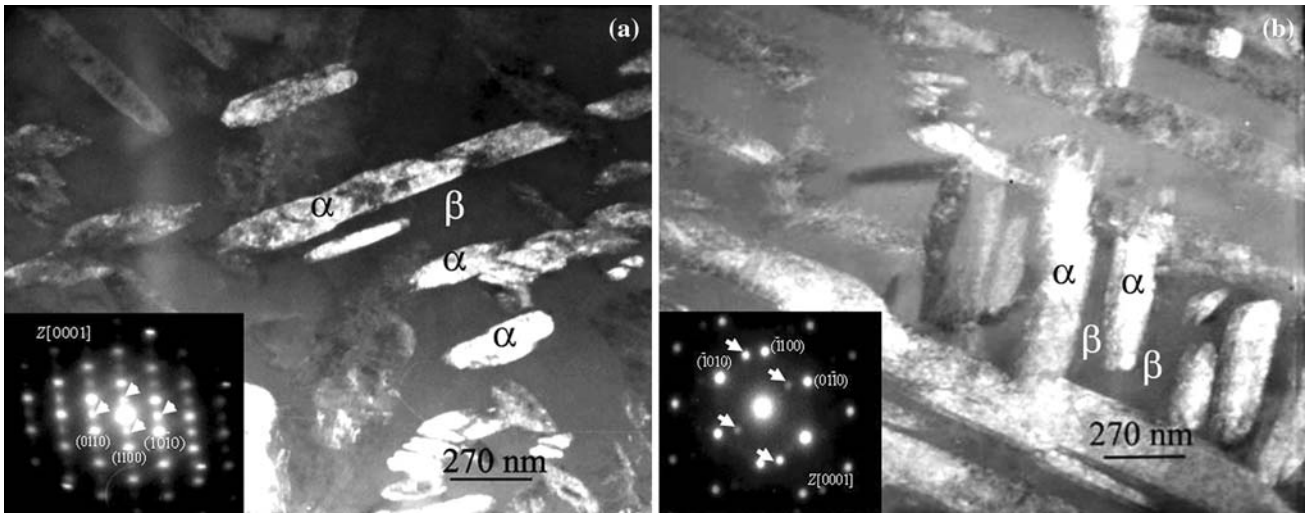

Fig. 13—TEM dark-field micrographs at HAZ and SAED pattern (as insert) of (*a*) 4HzPC-aged at 520 °C/10 h/AC and (*b*) 6HzPC-aged at 520 °C/10 h/AC. Figure (b) shows transformation product, alpha [0001], in retained beta matrix (indicated by arrows). Labels on the image correspond to respective phases.

cannot be accurately predicted with the preceding expression due to the nonisothermal nature of the thermal cycle imposed on the HAZ as well as the possibility of incomplete recrystallization. However, the ratio of grain sizes (≈3) is seen to be near to that estimated from the preceding expression (≈5), indicating the strong role of the thermal gradient in the HAZ microstructure. The discrepancy may be attributed to the difference in initial strain and the nonisothermal nature of the welding process.

B. *Alpha Precipitation*

Precipitation of α phase in β titanium alloys is being actively studied. Most of these studies are limited to multistep isothermal cycles of heat treatment and deformation. The α phase is expected to nucleate at β grain boundaries (α_{GB}) and grow normal to the grain boundary to a critical width beyond which Widmanstätten plates of the α phase (α_{WGB}) nucleate sympathetically and grow inward.[20] The appearance of α_{WGB} involves the nucleation of a precipitate crystal with a composition different from that of the matrix, at the interphase boundary of another crystal of the same phase. This observation made in β-CEZ[19] and other β-Ti alloys such as Ti-6.6 at. pct Cr and Ti-8.6 at. pct Mo alloys[29] can be noticed in this alloy too (Figure 8). This type of nucleation has been observed to occur frequently in a considerable variety of Fe-base, Cu-base, and Ti-base alloys. The compositional variation (Table II) in V, Cr (β stabilizer), and Al (α stabilizer) content across the precipitates corroborates previous observations in other systems.

Precipitation of α is expected to be also in the interior of the grain at locations where dislocation density is high or a subgrain boundary exists. The morphology of such precipitates changes from aggregate of α to lath when the aging temperature is increased beyond 723 K.[22] The EBSD micrographs (Figure 14(a)) of as-welded samples show aggregate morphology, while the aged samples show lath morphology of α phase (Figure 14(b)). In these orientation images, the step size used was 0.1 μm and edge grains were excluded from analysis. The analysis supports the idea that prior β-α transformation during the as-welded condition can result in finely distributed α along the β grains in the aged condition. Moreover, α lamellae between β phases is enriched in α-stabilizer species. The volume fractions of α phase indicated in the image could be an overestimate, because the size of the precipitates, as characterized by TEM, is much lower than the resolution limit of the EBSD system used. The black regions where the orientation could not be correctly identified hint that the α precipitates in as-welded condition are submicron in length scale.

Table II. TEM-EDX Composition (Weight Percent)

Condition	EDX Spot Location	Ti	V	Cr	Al	Sn
4HzPC aged	alpha lath	82.7	3.7	0.7	5.5	7.4
	beta matrix	66.7	20.3	5.1	3.2	4.6
6HzPC aged	alpha lath	83.1	3.9	0.7	6.9	5.4
	beta matrix	68.4	20.1	4.4	3.2	3.9

The X-ray diffraction pattern (shown in Figure 15) also complements the earlier findings of the presence of α phase in the aged samples. Indexed X-ray diffraction patterns of the aged samples show α peaks, whereas in as-welded samples, only β peaks are observed. The profiles of as-welded samples do not show peaks corresponding to α phase, indicating that their volume fraction is less than around 5 pct.

C. *Correlation with Mechanical Properties*

The tensile failure of as-welded specimens was in the FZ, indicating that the strength corresponds to that of

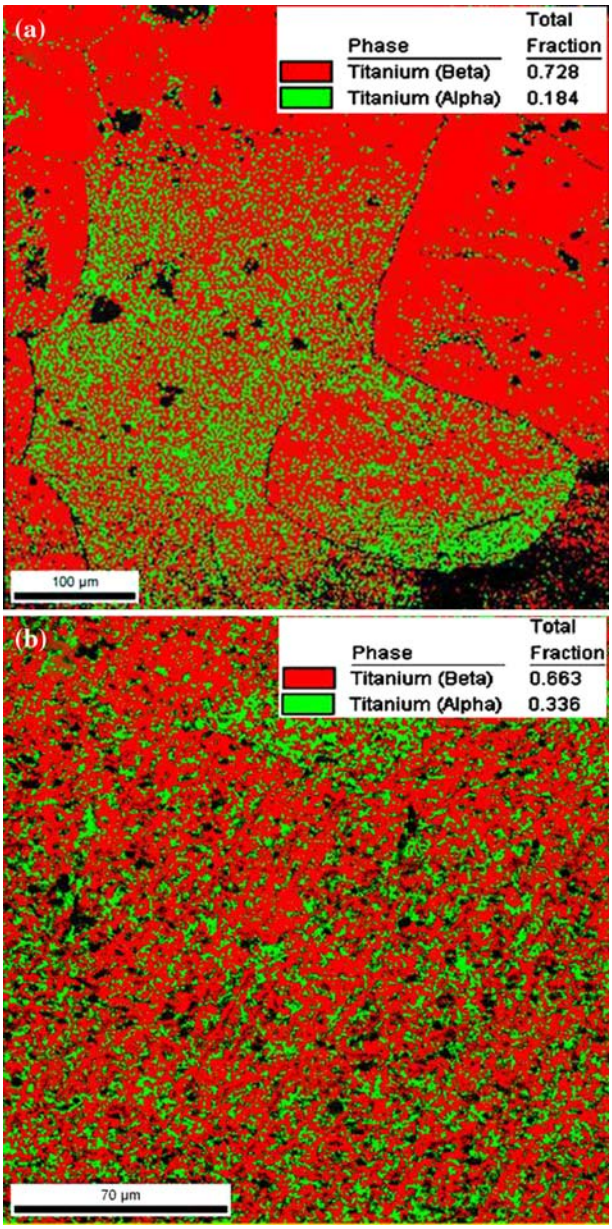

Fig. 14—EBSD phase map at HAZ of 2HzPC (*a*) in as-welded condition and (*b*) 520 °C/10 h–aged condition.

the FZ. However, the failure of the postweld heat-treated sample was in the base metal. Thus, the measured tensile properties could be a lower bound for the FZ and the HAZ. Figures 9 and 10 show that the highest strengths as measured by microhardness tests as well as transverse tensile tests are for the sample welded with a pulse frequency of 4 Hz. This is also the processing condition during which the measured thermal profile showed the highest temperature in the HAZ as well as thermal gradients. Since the traverse speed of the welding torch was kept constant for all conditions, this also implies the highest cooling rate for the 4 Hz sample. The length scale of the α platelets is the finest in the 4 Hz sample. The size and distribution of precipitates in identically postweld heat-treated samples of

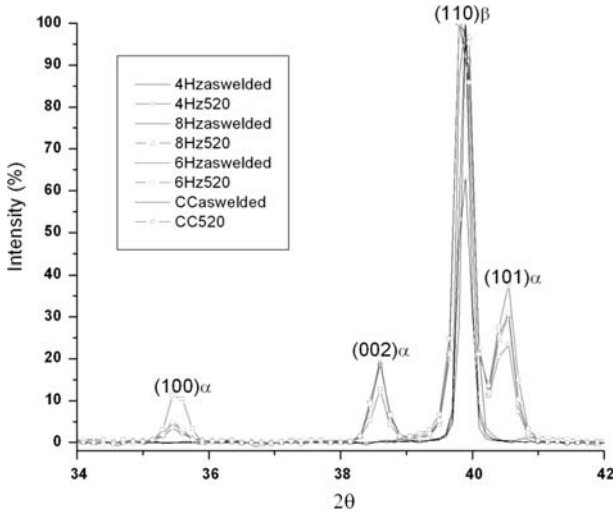

Fig. 15—XRD comparison as welded and aged at 520 °C/10 h.

4 Hz and 6 Hz showed that the size of α laths is smaller in 4 Hz (Figure 13). This also hints at a higher density of heterogeneous nucleation sites within the grains of 4 Hz weldment (Figure 14(a)). The maximum thermal gradient measured for this condition is the reason for the fine length scale of the microstructure leading to the high strength of this sample. Thus, the maximum strength of the 4 Hz weldment observed can be attributed to the smallest length scale of microstructure that could be rationalized by the thermal profile measured.

Significant improvement in the strength has been observed in the postweld heat-treated samples. The results presented are for the weldment with maximum strength in the as-welded condition. This improvement in strength and concurrent loss in ductility can be attributed to the two-phase microstructure with submicron length scale of α precipitates.

V. CONCLUSIONS

1. *In-situ* temperature measurement during welding shows that the temperature gradients of the PC conditions were found to be greater than those of the CC condition, since constant heat input is maintained in all cases.
2. Transmission electron microscopy confirms α precipitation with the finest length scale for the sample that underwent the steepest thermal profile (4 Hz PC).
3. Postweld aging within the β transus temperature resulted in α precipitation along the prior β grain boundary and lenticular α grown from the boundary toward the interior of the β grains. The size and spacing of lath precipitates of α within the grains also depend on the thermal profile experienced by the weldment.
4. Compositional variation exists between the β matrix and α laths. Depletion of β stabilizers, such as V, Cr along α laths, and depletion of the α stabilizing element, Al along the β matrix, are found to be predominant.

5. Finer sizes and distribution of α phase within the grains are correlated to the highest strength that could be observed in the weldments.
6. Postweld heat treatment of weldments resulted in significant improvement in tensile strength and a loss in ductility.

ACKNOWLEDGMENTS

This study was financially supported by a project from the ISRO-IITM cell. The authors thank Professor S.D. Pathak and Dr. M. Nageswara Rao for many useful discussions. The authors gratefully acknowledge R & D, TISCO (Jamshedpur), for providing permission to use their Gleeble facility during this study.

REFERENCES

1. S. Ankem and C.A. Greene: *Mater. Sci. Eng. A*, 1999, vol. 263, pp. 127–31.
2. S.M. Kazanjian and E.A. Starke, Jr.: *Int. J. Fatigue*, 1999, vol. 21, pp. S127–S135.
3. R.R. Boyer: in *Beta Titanium Alloys in the 1990's*, D. Eylon, R.R. Boyer, and D.A. Koss, eds., TMS, Warrendale, PA, 1993, pp. 335–46.
4. *Titanium '95*, The Institute of Materials, London, 1996, vol. II, pp. 988–95.
5. P.J. Bania: in *Beta Titanium Alloys in the 1990's*, D. Eylon, R.R. Boyer, and D.A. Koss, eds., TMS, Warrendale, PA, 1993, pp. 3–14.
6. J.G. Garland: *Met. Construc. Br. Weld. J.*, 1974, vol. 6, pp. 121–25.
7. H. Yamamoto, S. Harada, T. Ueyama, S. Ogawa, F. Matsuda, and K. Nakata: *Weld. Int.*, 1993, vol. 7, pp. 456–61.
8. G.M. Reddy, A.A. Gokhale, and K.P. Rao: *J. Mater. Sci.*, 1997, vol. 32, pp. 4117–26.
9. A.A. Gokhale, A.A. Tzavaras, H.D. Brody, and G.M. Ecer: *Proc. Conf. on Grain Refinement in Castings and Welds,* G.J. Abbaschian and S.A. David, eds., TMS-AIME, Warrendale, PA, 1983, pp. 223–47.
10. T. Shinoda, Y. Ueno, and I. Masumoto: *Trans. Jpn. Weld. Soc.*, 1990, vol. 21, pp. 18–23.
11. D.W. Becker and C.M. Adams, Jr.: *Weld. J.*, 1979, vol. 58, pp. 143s–147s.
12. T. Mohandas and G.M. Reddy: *J. Mater. Sci. Lett.*, 1996, vol. 15, pp. 626–28.
13. S. Sundaresan, G.D.J. Ram, and G.M. Reddy: *Mater. Sci. Eng. A*, 1999, vol. 262, pp. 88–100.
14. D.W. Becker and W.A. Baeslack III: *Weld. Res. Suppl.*, 1980, pp. 85s–92s.
15. W.A. Baeslack III, P.S. Liu, and T. Paskell: *Mater. Charact.,* 1993, vol. 30, pp. 147–54.
16. A.W. Sommer, S. Motokura, K. Ono, and O. Buck: *Acta Metall.*, 1973, vol. 21, pp. 489–97.
17. G. Terlinde and G. Fischer: in *Titanium and Titanium Alloys*, C. Lyens and M. Peters, eds., Wiley VCH GmbH, Germany, 2003.
18. S.J. Kim, B.H. Choe, and Y.T. Lee: in *Metallurgy and Technology of Practical Titanium Alloys*, S. Fujishiro, D. Eylon, and T. Kishi, eds., TMS, Warrendale, PA, 1994, pp. 167–72.
19. B. Appolaire, L. Heiricher, and E. Aeby-Gautier: *Acta Mater.*, 2005, vol. 53, pp. 3001–10.
20. J. Da Costa Teixeira, B. Appolaire, E. Aeby-Gautier, S. Denis, and F. Bruneseaux: *Acta Mater.*, 2006, vol. 54, pp. 4261–71.
21. P.K. Poulose and M.A. Imam: *Titanium '95*, The Institute of Materials, London, 1996, vol. II, pp. 988–95.
22. T. Furuhara, T. Maki, and T. Makino: *J. Mater. Process. Technol.*, 2001, vol. 117, pp. 318–23.
23. O.M. Ivasishin, P.E. Markovsky, S.L. Semiatin, and C.H. Ward: *Mater. Sci. Eng. A*, 2005, vol. 405, pp. 296–305.
24. N. Niwa and H. Takatori: in *Beta Titanium Alloys in the 1990's*, D. Eylon, R.R. Boyer, and D.A. Koss, eds., TMS, Warrendale, PA, 1993, p. 237.
25. H. Ohyama, H. Nakamori, Y. Ashida, and T. Maki: *ISIJ Int.*, 1992, vol. 32, pp. 222–31.
26. J. Ma and Q. Wang: *Mater. Sci. Eng. A*, 1998, vol. 243, pp. 150–54.
27. *Materials Properties Handbook: Titanium Alloys*, R. Boyer, G. Welsch, and E.W. Colings, eds., ASM INTERNATIONAL, Materials Park, OH, 1994, p. 901.
28. H. Ohyama and Y. Ashida: *ISIJ Int.*, 1991, vol. 31, pp. 799–806.
29. E.S.K. Menon and H.I. Aaronson: *Acta Metall.*, 1987, vol. 35, pp. 549–63.